



Numerical prediction of Péclet number in small-sized fixed bed reactors of spheres

Vittorio Petrazzuoli, Matthieu Rolland, Vasileios Sassanis, Vincent Ngu, Yves Schuurman, Lionel Gamet

► To cite this version:

Vittorio Petrazzuoli, Matthieu Rolland, Vasileios Sassanis, Vincent Ngu, Yves Schuurman, et al.. Numerical prediction of Péclet number in small-sized fixed bed reactors of spheres. Chemical Engineering Science, 2021, 240, pp.116667. 10.1016/j.ces.2021.116667 . hal-03246792

HAL Id: hal-03246792

<https://ifp.hal.science/hal-03246792>

Submitted on 2 Jun 2021

HAL is a multi-disciplinary open access archive for the deposit and dissemination of scientific research documents, whether they are published or not. The documents may come from teaching and research institutions in France or abroad, or from public or private research centers.

L'archive ouverte pluridisciplinaire **HAL**, est destinée au dépôt et à la diffusion de documents scientifiques de niveau recherche, publiés ou non, émanant des établissements d'enseignement et de recherche français ou étrangers, des laboratoires publics ou privés.

Numerical prediction of Péclet number in small-sized fixed bed reactors of spheres

Vittorio Petrazzuoli¹, Matthieu Rolland¹, Vasileios Sassanis¹, Vincent Ngu¹, Yves Schuurman²,
Lionel Gamet^{1*}

1 Process Intensification dept, IFP Energies Nouvelles, Rond-point de l'échangeur A7, 69360 Solaize, France

2 Univ Lyon, Université Claude Bernard Lyon 1, CNRS, IRCELYON, 2 Avenue Albert Einstein F-69626, Villeurbanne, France

**Corresponding author: lionel.gamet@ifpen.fr*

Abstract

Fluid dispersion in small fixed bed reactors under single phase laminar flow conditions is evaluated through accurate predictions of axial Péclet numbers Pe_{ax} using Direct Numerical Simulations (DNS). The fixed bed packing is obtained through the Discrete Element Method (DEM) code Grains3D. Pe_{ax} numbers are computed from steady state simulations of the flow. An additional set of equations solving the spatial distribution of the moments of the age distribution is used. This gives access to local information on dead zones or bypasses. Computations are realized with the OpenFOAM[®] open-source library. Results are close to the experimental data. The DEM-OpenFOAM[®] workflow benefits from an accurate control of the fluid physical properties and packing geometry, thus leading to a faster production of data than an experimental approach.

We first explore the influence of the reactor-to-sphere diameter ratio δ ($\delta < 4$), fluid velocity and molecular diffusivity on the Pe_{ax} number. The behavior proves much more complex than any previous report, and it can be qualitatively explained by looking at the packing structure. Then, we use the DEM-OpenFOAM[®] workflow to quantify the uncertainty on the Pe_{ax} number when

repeating the packing of a $\delta = 4$ fixed bed reactor, and we propose that the uncertainty on the Pe_{ax} number decreases as a function of the reactor length to the power of -0.5.

Key words (max 6): *Computational Fluid Dynamics; small fixed beds of spheres; axial Péclet number; Direct Numerical Simulations; laminar flow; moments of age*

1 Introduction

1.1 Fixed bed downscaling

Over the decades, fixed bed reactors for catalyst testing have faced a reduction in size. Nowadays they commonly have diameters below 1 cm, the limit being the catalyst pellet size (~1-3 mm). The advantages of these small reactors are numerous: less catalyst used, less amount of reactant used and of wastes produced, better temperature control, reduced safety risks and easier implementation of parallel reactor systems [1]. Those reactors were designed for catalyst screening, so that the hydrodynamics was not really an issue if the ranking and uncertainties were correct. As these reactors produce a large amount of data, a new question arises: can we use their results to build models for catalyst performance prediction? One of the limiting factors might be the hydrodynamic quality of the flow.

Downscaling of fixed bed reactors is usually performed by keeping the ratio of flow rate (Q) to the catalyst amount (V_{cat}) constant, usually denoted as Space Velocity or SV . This ratio can be seen as the inverse of the contact time. When expressing the catalyst amount as a volume, the SV is the ratio of the superficial velocity (u) to the reactor length (L) (Equation 1). Laboratory reactors are typically 10-50 cm long so that the velocities are 20-100 times smaller than in industrial reactors (~ 10 meters in length).

$$SV = \frac{Q}{V_{cat}} = \frac{u}{L} \quad \text{Equation 1}$$

For a wide range of reactions in biorefinery, biochemistry, petrochemistry, and refining, the velocities in laboratory reactors are so low that the flow regime is often laminar with Reynolds (Re) number lower than 10. For this reason, we focus on single-phase laminar flows in the rest of the paper.

Currently, the reactors used in heterogeneous catalyst testing have diameter values smaller than 1 cm and lengths that usually do not exceed 20-30 cm. As the catalyst particles are on the order of a few millimeters, these reactors are usually operated with values of $\delta = D_r/d_p$ (reactor/sphere diameter ratio) between 1 and 5, possibly 10, while traditional packed beds have often larger values. In packed bed millireactors, the ratio δ governs the disposition of the particles in the reactor. For large values of δ there are few preferential paths and dead-zones due to the stochastic position of the particles at the center of the bed and the higher packing density [2, 3], while for the low δ values, occurring in packed bed millireactors, the global void fraction is higher and radially non-uniform [4], and preferential paths near the walls are significant and drive most of the flow.

1.2 Plug flow behavior

To perform kinetic studies, the results of the experiments must express the kinetic behavior of the catalyst rather than the hydrodynamics of the reactor. In a fixed bed, the ideal flow is plug flow with high heat and mass transfer coefficients. If these conditions are not met, the usual approach is to characterize those features building a reactor model that accounts for them and then optimize a kinetic model coupled with the reactor model. An example of this process can be found in [5]. In this paper, we focus on the plug flow behavior of the fixed bed reactors that is

very well described by a classical convection equation augmented with an axial dispersion term (Equation 2) [6]:

$$\frac{\partial c}{\partial t} = D_{ax} \frac{\partial^2 c}{\partial z^2} - \frac{u}{\varepsilon} \frac{\partial c}{\partial z} \quad \text{Equation 2}$$

in which z is the axial coordinate along the bed, c is the concentration of the species, D_{ax} the axial dispersion coefficient, u the superficial gas velocity, ε the void fraction of the reactor and t the time. If the axial dispersion coefficient, D_{ax} , is sufficiently small, the axial dispersion can be neglected, which greatly simplifies the models. At this point, it is worth introducing the Pe_{ax} number (Equation 3) that compares dispersion time scales to the axial convective time scales:

$$Pe_{ax} = \frac{u \cdot L}{\varepsilon \cdot D_{ax}} \quad \text{Equation 3}$$

in which L is the reactor length. The higher the Pe_{ax} number, the closer the reactor is to ideal plug flow. In kinetic studies, it is very interesting to operate reactors with Pe_{ax} number “large enough” so that they can be considered as ideal. The “large enough” term depends on the conversion level of the reaction as proposed by Mears [7].

1.3 Experimental literature

To experimentally evaluate the dispersion in the reactors, transient experiments are required. Usually a tracer is injected, and its concentration temporal evolution is recorded at the reactor outlet. When the inlet is a Dirac function, the outlet curve is the residence time distribution (RTD) curve, denoted as $E(t)$. This is the reason why these types of experiments are often called RTD measurements. In practice, the inlet is never an exact Dirac function so that a measurement of the reactor inlet is recommended.

The axial dispersion coefficient can be deduced from the reactor outlet (and inlet) temporal tracer concentration profiles by solving the axial dispersion model equation [8–12].

Plug flow behavior studies in packed bed millireactors are scarce. A common rule-of-thumb [6] in chemical engineering recommends values of δ higher than ~ 15 , so that the radial porosity fluctuations near the walls have less impact on the average flow and the packing can be considered uniform in the radial direction. In this case, variations of the fluid velocity, reactor porosity and axial dispersion coefficient in the radial direction can be neglected. Packed bed millireactors do not follow this rule of thumb and another design criterion is required.

Studies from Šolcova and Schneider [10], Scott et al. [13] and Hsiang and Haynes [14] showed that, in terms of plug flow behavior, similar results to those observed in larger packed beds are achieved when δ is below 2. A previous study of our work group [15] investigated the effect of δ on the Pe_{ax} number, concluding that the behavior is not monotonic, but the experimental limits on the control of the fluid physical properties and the packing geometrical parameters did not allow us for a more detailed understanding.

Good control of the experimental setup is necessary to achieve a good accuracy on the axial dispersion measurements, which is time consuming [15]. Besides that, not all experimental conditions can be tested: spherical beads are only available in limited number of diameters, same for the reactor diameters. Fluid and tracer choice are limited by the analyzer's capabilities.

1.4 CFD in fixed beds

Direct Numerical Simulation (DNS) of reactive flows in fixed beds has progressed enormously in the last decade with velocity, concentration and temperature 3D profiles [16–18]. Many papers present workflows to solve CFD problems in random packed beds of complex shapes, some of

them using open source solvers like OpenFOAM[®] [19–21]. The computational resources are now sufficient to successfully perform DNS of packed bed High Throughput Experimentation reactors for non-reactive single-phase flows.

However, transient CFD simulations are still expensive and few works focused on fluid dispersion in small-sized fixed bed reactors. Among them, a CFD study simulating residence time curves from Müller et al. [22] on a Single Pellet String Reactor (cylindrical reactor and spherical particles, $\delta = 1.2$ and $L = 0.1$ m) concluded plug flow behavior for all the conditions tested, ranging from laminar to turbulent flow. Then, Fernengel et al. [23] performed a similar study for δ value ranging between 1.125 and 1.75. Non-diffusive numerical tracer simulations revealed that the reactors have plug flow behavior. They also simulated a heterogeneously catalyzed isothermal and isomolar gas-phase reaction with no change in gas density that showed conversions deviating less than 5% from plug flow.

1.4.1 Theory of moments of age distribution

A very interesting advance comes from the work of Liu and Tilton [24] that showed that the moments of age spatial distribution could be computed using steady-state simulations. Let us first introduce the notion of age distribution. At any point of the reactor, the age of the molecules $a(x,t)$ since the reactor entrance follows a distribution, which is generally unknown but can be characterized by its moments (Equation 4).

$$M_n(x) = \frac{\int_0^{+\infty} t^n \cdot a(x,t) dt}{\int_0^{+\infty} a(x,t) dt} \quad \text{Equation 4}$$

Following the works of Spalding [25], Danckwerts [26] and Zwietering [27], Liu and Tilton [24] demonstrated that the n -th moment of the age distribution follows a steady state convection/diffusion equation similar to momentum, energy or species:

$$\nabla \cdot (\mathbf{v} \mathbf{M}_1) = \nabla \cdot (\mathbf{D}_m \nabla \mathbf{M}_1) + 1 \quad \text{Equation 5}$$

$$\nabla \cdot (\mathbf{v} \mathbf{M}_n) = \nabla \cdot (\mathbf{D}_m \nabla \mathbf{M}_n) + n \mathbf{M}_{n-1}, n > 1 \quad \text{Equation 6}$$

in which \mathbf{v} is the velocity vector and \mathbf{D}_m the molecular diffusion coefficient. The boundary conditions are: $M_i = 0$ at inlet, null fluxes at the reactor walls and outlet. The equation for the first moment is quite easy to understand. The first moment of age follows a classical convection diffusion equation and its rate of change is unity. Those equations are valid for any open reactor, i.e. with an inlet and an outlet, and are easy to implement and solve in steady-state CFD solvers. Liu and Tilton also demonstrated that a mass flux weighted integration of the M_1 and M_2 fields over the inlet and outlet (Equation 7) yields $M_{1,x}$ and $M_{2,x}$. The Pe_{ax} number can be then calculated using Equation 8.

$$\mathbf{M}_{i,x} = \frac{\int_x \mathbf{u} \cdot \mathbf{M}_i \cdot d\mathbf{S}}{\int_x \mathbf{u} \cdot d\mathbf{S}}, \quad i=1 \text{ or } 2, x = \text{inlet or outlet} \quad \text{Equation 7}$$

$$Pe_{ax} = 2 \frac{\bar{t}^2}{\sigma^2} = 2 \frac{(\mathbf{M}_{1,outlet} - \mathbf{M}_{1,inlet})^2}{(\mathbf{M}_{2,outlet} - \mathbf{M}_{1,outlet}^2) - (\mathbf{M}_{2,inlet} - \mathbf{M}_{1,inlet}^2)} \quad \text{Equation 8}$$

in which \bar{t} is the mean residence time, σ^2 is the variance and M_1 and M_2 are the first and second order moments of spatial distribution of age.

Another dimensionless number widely used in literature for the quantification of fluid dispersion is the Bodenstein number (Bo). The difference between the Bo and Pe_{ax} numbers consists only in the characteristic length, which is the particle diameter (d_p) for the Bo number. The Bo number can thus be calculated from the Pe_{ax} number using Equation 9:

$$Bo = \frac{Pe_{ax} \cdot d_p}{L} \quad \text{Equation 9}$$

The integrals of the moments (Equation 7) can also be easily computed in cross-sections of the reactor located at various axial position z ($z = 0$ at the bed inlet, $z = L$ at outlet). In this way, considering the first and second order moments integrals, it is possible to obtain the profile of the Pe_{ax} or Bo number along the bed axis.

1.5 Aim of the present work

The novelty of the present work is in the application of the Liu and Tilton moments of the age distribution theory [24] for steady state simulations of the hydrodynamics of small-sized fixed beds with low reactor-to-sphere diameter ratio δ . We focus on the area $\delta < 4$, not yet fully explored in the literature.

We calculate the Pe_{ax} and Bo numbers as a post-treatment of a combined open-source workflow (DEM packing & CFD). We will study the effects of different physical, process and geometrical parameters and the uncertainty on the Pe_{ax} number induced by randomly repeating the packing. The CFD is simple: laminar flow (Navier-Stokes equations) augmented with two convection – diffusion equations for the moments of age. In the following sections, we will present the workflow in detail as well as its validation.

2 Numerical methods

2.1 Detailed simulation workflow

The simulation workflow starts with the reproduction of the particle's arrangement using a Discrete Element Method (DEM). The DEM method [28] is a Lagrangian particle tracking method which computes the velocity, trajectory and orientation of each individual particle in the system. The simulation accounts for the collisions of each particle with other particles and with

the system walls. A key feature of any DEM tool is its ability to detect collisions, determine the contact point(s) and compute the resulting contact forces. Our DEM code Grains3D is based on the Gilbert-Johnson-Keerthi algorithm for collision detections [29]. Detailed information about our code Grains3D, its DEM and parallel computing features including the contact force model and the extension to non-convex shapes, can be found in the publication of Wachs et al. [30]. In the present work, we used Grains3D to compute packings of spheres in cylindrical reactors. Simulations for this work were run on a single CPU and lasted a few hours at most.

Meshing is performed using the sequence of `blockMesh` and `snappyHexMesh` OpenFOAM® utilities. `blockMesh` computes the background mesh, which defines the refinement level 0. Its output is a fully hexahedral grid consisting of nearly cubic cells, arranged in a butterfly, structured blocks topology to match the reactor cylindrical shape. The butterfly topology is obtained with an H-grid block around the cylinder axis, and with O-grid blocks at the reactor walls. The background grid refinement (level 0) is a significant parameter on the simulation results. In this paper, we present results in terms of “density”, which is the number of grid cells per diameter of reactor (*cpd*).

`snappyHexMesh` computes a refined grid that matches the solid interfaces of the particles and the reactor walls. The particles are introduced in the geometry section of `snappyHexMesh` as “searchable objects”. This feature enables to define the spherical particles analytically instead of using triangulated surfaces in STL format. Local refinements are specified on solid surfaces and small gaps. Refinements are performed by specifying a grid level in `snappyHexMesh`. For example, a grid level 1 on the walls (particles and reactor) corresponds to a division by a factor 2 of the background grid cell size, which is the level 0 defined by `blockMesh`. An additional gap

level increment of 1 can be used. This parameter is only applied in regions of small gaps, where the spherical particles are tangent. The output mesh consists in a mostly hexahedral grid, except near the walls where tetrahedral and polyhedral cells can occur due to the projection of cell faces on the walls. The interested reader can refer to the OpenFOAM[®] online user-guide [31] for more details.

A suitable set of parameters has been chosen to achieve mesh convergence with the minimum mesh size. This is detailed in the mesh convergence section.

The next step in our workflow is to compute the velocity and the first two moments of age distribution in the packed beds. We used the open source OpenFOAM[®] suite as other work groups [19, 20]. The solver is a laminar incompressible steady-state flow solver using the SIMPLE pressure-velocity coupling algorithm, namely `simpleFoam` [32], augmented with two convection diffusion equations for the moments M_1 and M_2 with a source term as described in section §1.4.1. Our implementation of the mean age equations was validated against the 2D test case detailed in Liu and Tilton [24], which is not presented here. Boundary conditions are defined as follows: velocity is uniform on the inlet surface, pressure is uniform on the outlet surface, first and second moments are uniform and equal to 0 on the inlet surface and with no gradient on the outlet surface. On the reactor walls and particles, we assumed no-slip condition for the velocity and null gradient for the moments of the age M_1 and M_2 .

We use second order spatial schemes for all the computations. The Gauss linear scheme is used for gradient terms, with a cell limiter that limits the gradient such that, when cell values are extrapolated to faces using the calculated gradient, the face values do not fall outside the bounds of values in surrounding cells. Laplace operators are discretized with the Gauss linear corrected

scheme. The convective term in the momentum equation is treated with a bounded Gauss linear upwind scheme specialized for vector fields. This scheme reduces to an upwind scheme in regions of strong velocity gradient. The vector specialization consists in calculating a single limiter which is applied to all components of the vectors, rather than calculating separate limiters for each component. Finally, scalars like the moments of age, are computed using an upwind first order scheme. In terms of linear solver, the generalized Geometric-Algebraic Multi-Grid (GAMG) solver was used for the pressure equation. The iterative smooth solver was used for other variables. All linear solvers used a Gauss-Seidel preconditioner. We refer the reader to the OpenFOAM[®] user's guide [33] for more details on numerical schemes.

Last, the integrals of the moments are computed in a post-processing step using a function object that computes the mass flux weighted integrals of the moments over planar cross sections at various positions along the axial direction z of the reactor.

2.2 Mesh convergence

The mesh convergence is evaluated by checking the accuracy of the simulations on known global quantities such as flow rate conservation, total particles volume, and mean residence time. Those numbers are correlated. We next check the mesh convergence on pressure and Pe_{ax} number. A parametric search shows that for our problem, the optimal mesh is obtained with a fine background mesh and moderate additional refinement (level 1 in the `snappyHexMesh` terminology) near the solid surfaces and in the small gaps. This is an expected behavior for our problem in which we need to capture the velocity gradients near the solid surfaces and the concentration gradients everywhere in the volume. To better capture flow boundary layers, `snappyHexMesh` has a feature to add prismatic cell layers on walls, of prescribed thickness

and growth ratio. Layers addition proved unnecessary in the presented cases, due to the low Re number simulated.

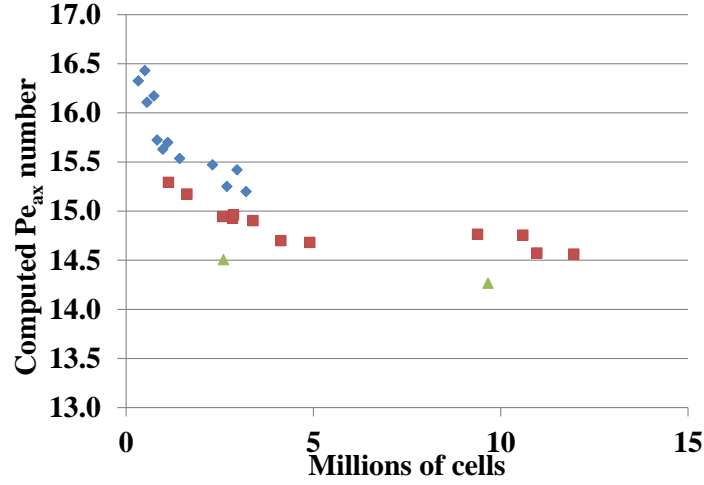


Figure 1. Mesh convergence on Pe_{ax} number as a function of the total grid size for three background cell densities. $L = 50$ mm, $D_r = 7.75$ mm, $d_p = 4$ mm, $u = 0.0272$ m/s and $D_m = 10^{-6}$ m²/s. Blue diamonds: 27 cpd, red squares: 54 cpd, green triangles: 80 cpd. All the points of the same color and shape correspond to meshes of same cpd but different level of refinement on particles, walls and in small gaps. Selected grid: green triangle with the smallest number of cells

The chosen mesh is the one with 80 cells per reactor diameter, with only a moderate additional refinement near the solid surfaces and in the small gaps. This corresponds to the green triangle with the lowest number of cells in Figure 1. The mesh is presented in Figure 2. The mesh convergence has been checked on 4 geometries: $D_r = 7.75$ mm and particles $d_p = 7.5$ mm, $d_p = 4$ mm, $d_p = 3$ mm and $d_p = 2.4$ mm for each fluid velocity and molecular diffusivity tested.

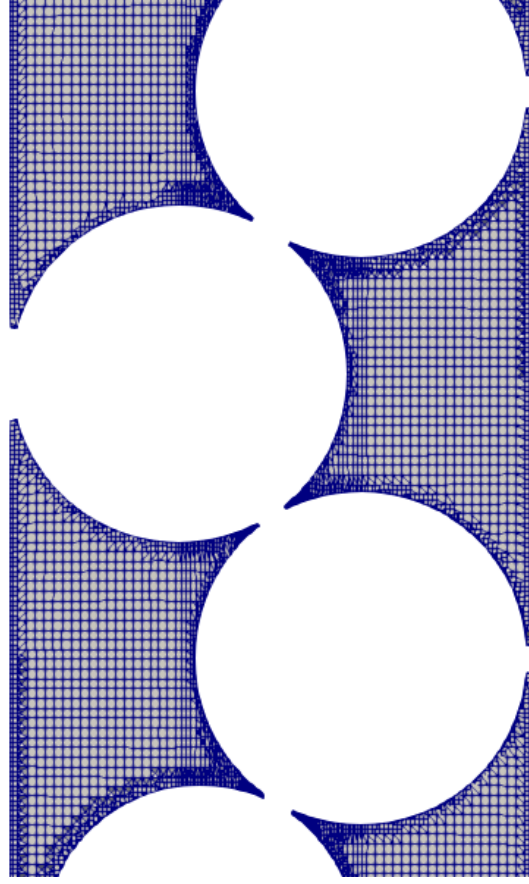


Figure 2. Cut of the mesh obtained with the final meshing strategy. $D_r=7.75$ mm, $d_p = 5$ mm

Numerical convection - diffusion problems can be quite stiff, requiring fine mesh near the catalyst pellets. However, in our case, mesh convergence proved easier than expected. The mean age evolves almost linearly from the entrance to the outlet while the second moment presents a quadratic shape (see Figure 3). The problem is numerically smooth and the mesh reasonable in size. A typical simulation of the flow, including moments, lasts 10 hours on 48 cores.

The automatic meshing workflow described above can naturally lead to bridges in regions of small gaps, like near the points of tangency between spheres or between a sphere and the reactor wall (see Figure 2). This question has been studied by Dixon [34] and is also briefly discussed by Boccardo [20]. As the current study only concerns hydrodynamics, no particular treatment was

needed to handle the bridges created by `snappyHexMesh`. A special treatment would have been necessary at the contact points if we had to solve heat transfer physics [34]. From a practical point of view, the gap level increment parameter discussed in section §2.1 controls the level of refinement in small gap regions. Based on pressure gradient prediction and axial Péclet numbers, we verified that increasing this parameter beyond the value 1 used in this study did not change the obtained results. Mesh convergence was thus obtained with a gap level increment of value 1. Moreover, the porosity of the bed obtained numerically was found within 0.4% of the theoretical porosity.

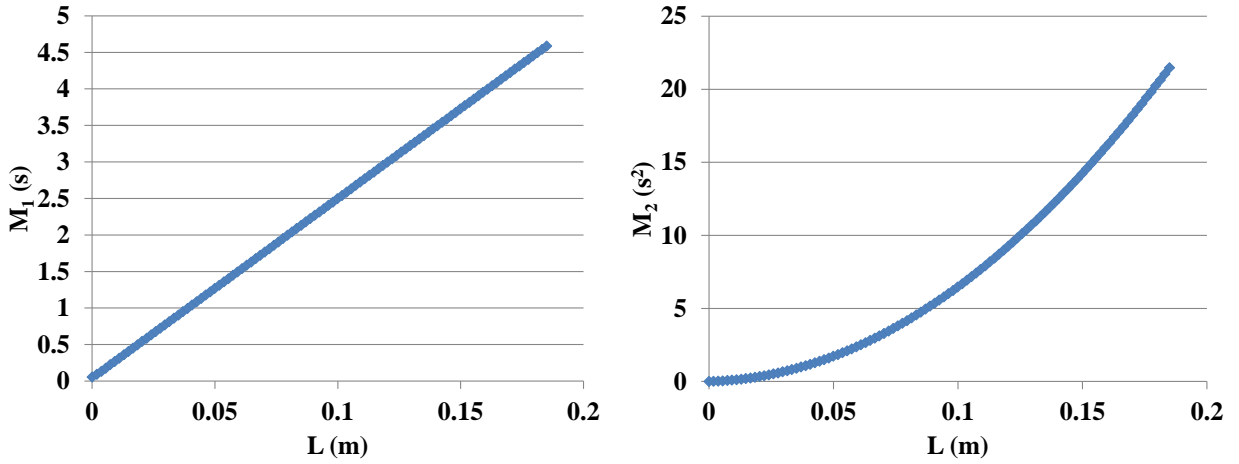


Figure 3. Example of M_1 and M_2 evolution along the bed. $D_r = 7.75$ mm, $d_p = 5$ mm, $u = 0.0272$ m/s, and $D_m = 7.5 \times 10^{-5}$ m²/s

2.3 Workflow validation

We validated the predictive ability of our workflow (DEM+CFD with OpenFOAM[®]) with experimental estimations of the Bo numbers performed in a 7.75 mm diameter reactor. The comparison of the Bo numbers is equivalent to the comparison of the Pe_{ax} numbers, since there is

only a scale factor between these two dimensionless numbers (see Equation 9). Apparatus and procedures are described in the article of Petrazzuoli et al. [15].

Numerical simulations are performed using the corresponding physical properties and operating conditions: $0.014 < u < 0.028$ m/s, $D_r = 7.75$ mm, $D_m = 7.5 \times 10^{-5}$ m²/s (helium-nitrogen diffusivity), $\rho = 1.2$ kg/m³, $\mu = 1.85 \times 10^{-5}$ m²/s (nitrogen properties) for various particle diameters.

As it can be seen from Figure 4, the agreement is good except for the data corresponding to the reactor with $\delta = 1.1$, which corresponds to the lowest δ value explored in this comparison. The experimental data have been confirmed by repeating twice the experiments, while a mesh refinement confirmed the CFD results. The origin of this difference is unclear. Small differences between experimental and numerical geometries (local deviation of reactor diameter, particle diameter and sphericity...) are likely to be more significant in this case than in the others. In the case of $\delta = 1.1$, we have only one sphere per diameter (a Single Pellet String Reactor, SPSR). In SPSRs, the fluid flow mainly passes in the empty space between the particles and the reactor wall. As for $\delta = 1.1$ we have the largest spheres among the ones considered in this comparison, we have thus the smallest passage at the reactor wall. Any experimental error in the particle sphericity or in the reactor diameter would thus be more influent in this case. This could explain the differences observed in the fluid dispersion, leading to differences between experimental and numerical *Bo* numbers.

A last comment can be that simulations may not solve the right equations because of higher *Re* number values so that the flow is no longer laminar. The *Re* number, based on the particle diameter as characteristic length, is larger than 20 for the data that do not match. Moreover, for

non-laminar flows, the molecular diffusion term of Equation 5 and Equation 6 is no longer valid. Even though the origin of the discrepancy is not exactly known, we decided to present anyway the obtained data. We need to keep in mind that for very low values of δ (< 1.2) the experimental-CFD matching is probably less accurate.

However, CFD is able to capture changes in trend near $\delta = 2$, as we will see later. In fact, simulations confirmed that the experimental data were correct and made us stop looking for loopholes in our experimental setup.

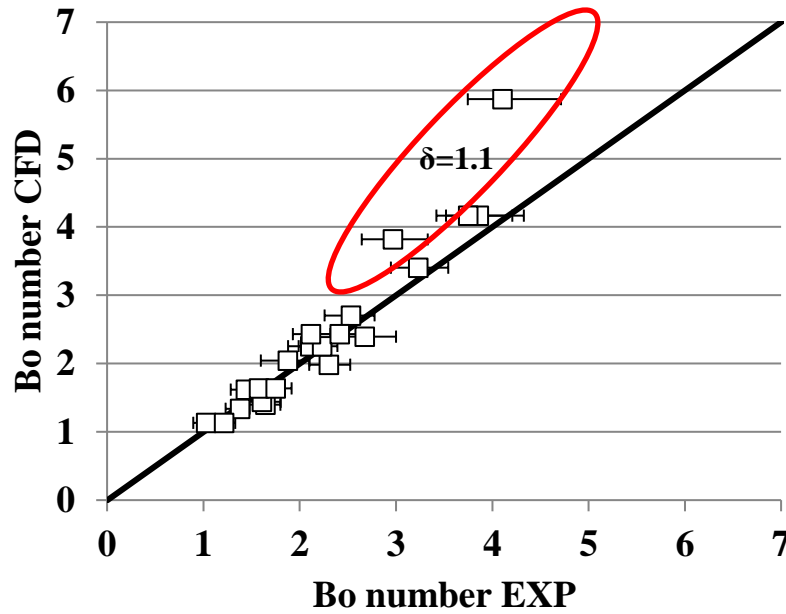


Figure 4. Validation of the CFD workflow by comparing the Bo number values of simulations and experiments. $D_r = 7.75$ mm. Comparison for different values of u (0.014, 0.021 and 0.28 m/s) and δ (1.1, 1.29, 1.55, 1.93, 2.58, 3.875)

Another validation was performed against the experimental data from Šolcova and Schneider ([10], Figure 5). The agreement is also good. We observe a small overestimation of the Bo numbers, particularly for high Pe_m numbers (Equation 10).

$$Pe_m = \frac{u d_p}{\varepsilon D_m} \quad \text{Equation 10}$$

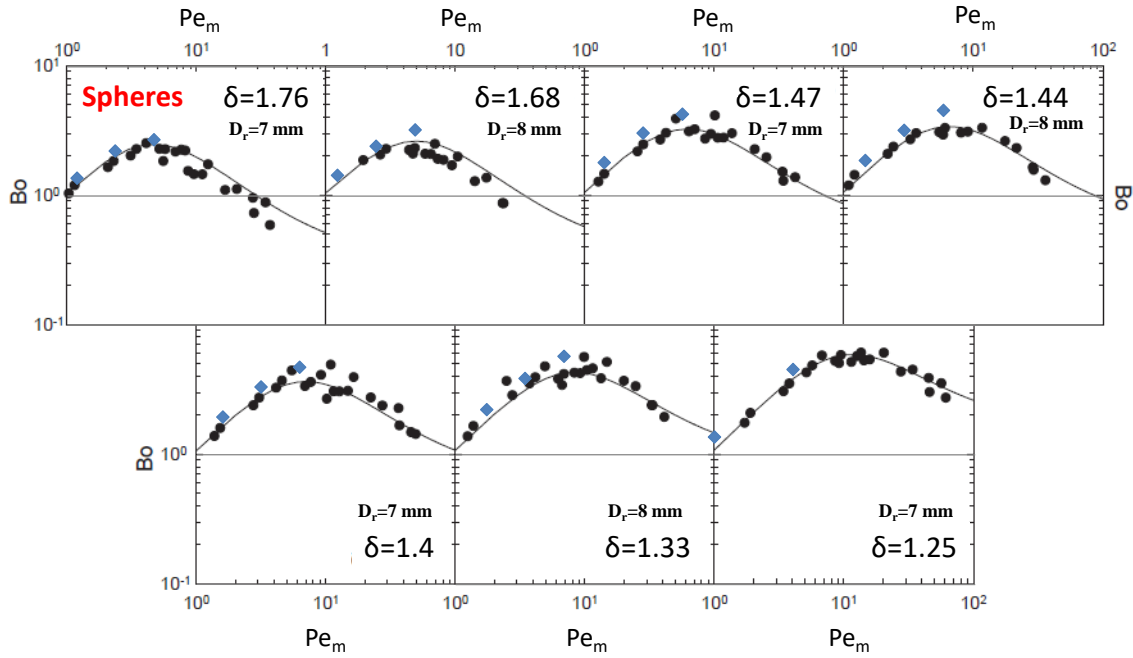


Figure 5. Comparison of our CFD results (in blue) with Šolcova and Schneider (in black) [10]

We conclude that our workflow correctly predicts the Bo numbers, except for low δ values in which we observe overestimations. Simulations take less than 24 hours and can be fully automated with scripts. Through parallelization, they yield results faster than experiments. An additional benefit of the DEM + CFD workflow is that we have a good control of the simulation parameters, especially geometrical dimensions and fluid properties.

3 Results

We used the CFD simulations to gain a better understanding about two crucial questions in heterogeneous catalyst testing. The first issue deals with the evolution of the Pe_{ax} number as a function of δ in small reactors filled with spherical beads. The experimental data presented in [15] show a complex behavior with δ that we wanted to explore more in detail. We used *in silico* experiments to estimate Pe_{ax} numbers for different values of δ and other physical parameters (molecular diffusivity) and process parameters (fluid velocity, particles diameter, reactor diameter and length). We report this in section §3.1.

The second issue is about the repeatability of the Pe_{ax} number when repeating the packing. In a previous work we showed that 10% variability on void fraction has to be expected [35] when randomly repeating the packing with the same particles. What is the effect on the Pe_{ax} number when repeating a random packing? We use the predictive capability of our workflow to repeat the simulation starting from the packing generation using another random seed. This is explored in section §3.2.

3.1 Axial Péclet number in narrow reactors

3.1.1 Axial Péclet number evolution along the bed

Equation 8 can be generalized between any two axial positions z_1 and z_2 (with $z_1 < z_2$) in the bed:

$$Pe_{ax}(z_1 \rightarrow z_2) = 2 \frac{(M_{1,z_2} - M_{1,z_1})^2}{(M_{2,z_2} - M_{1,z_2}^2) - (M_{2,z_1} - M_{1,z_1}^2)} \quad \text{Equation 11}$$

The $Pe_{ax}(z_1 \rightarrow z_2)$ number can be seen as a “local” Péclet number between two axial coordinates. For z_1 chosen as the bed inlet, and $z_2 = z$, $Pe_{ax}(z)$ should vary linearly along the bed axis coordinate z . $Pe_{ax}(z)$ is shown on Figure 6 for a bed with $\delta = 1.55$. Depending on the

value of molecular diffusivity D_m , the $Pe_{ax}(z)$ number evolution is slightly different. For higher values of molecular diffusivity ($>10^{-5} \text{ m}^2/\text{s}$) the $Pe_{ax}(z)$ number follows an almost perfect straight line, as theoretically expected (see Figure 6, A), while for lower values ($<10^{-5} \text{ m}^2/\text{s}$) the behavior presents some “staircases” around the linear trend (see Figure 6, B). Local packing structures of the spherical particles are at the origin of this staircase effect on local Péclet number variations. Packings can locally present either bypasses or dead zones, depending on the local void fraction and on the local configuration of the contact points and channels between the spheres. The CFD results shown in Figure 6 reveal that behavior, particularly for low values of molecular diffusivity.

Finally, when computing the overall bed Pe_{ax} number ($z_2=z_{outlet}$), this is found to be proportional to bed length as experimentally observed (see Petrazzuoli et al. [15]).

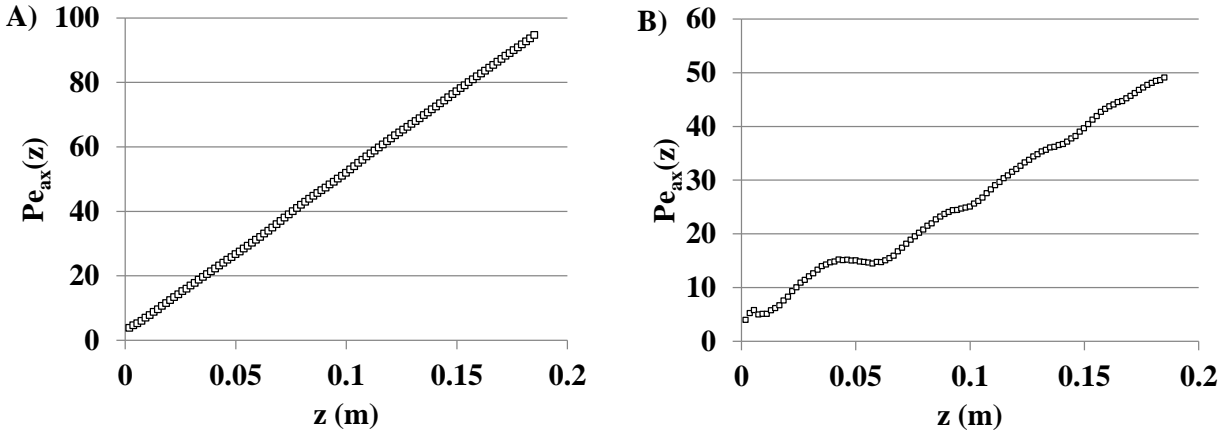





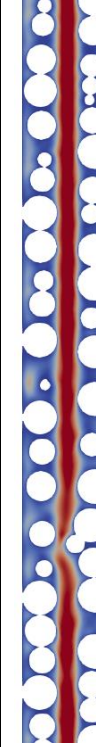
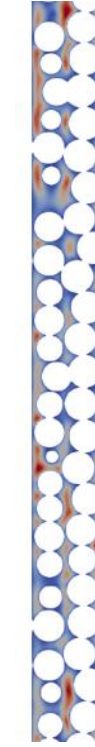
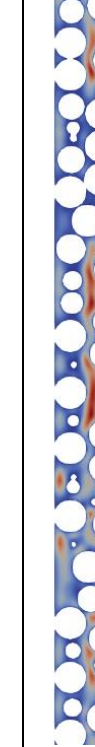

Figure 6. $Pe_{ax}(z)$ number evolution along the bed axis z for two different molecular diffusivity values: A) $D_m = 8 \times 10^{-5} \text{ m}^2/\text{s}$, B) $D_m = 10^{-6} \text{ m}^2/\text{s}$. $D_r = 7.75 \text{ mm}$, $d_p = 5 \text{ mm}$

3.1.2 A close look at the local packing structures

Table 1 shows the packing structures and the flow fields of some of the CFD simulations. For $\delta < \delta_c$, with $\delta_c = 1 + \sqrt{3}/2 = 1.87$, a particle touches the wall and 2 other particles (one above, one below). The particles arrange in a planar and alternate way. Two side passages are present on the side of the particles. At the critical value $\delta = \delta_c$, the reactor is wide enough so that the particle has now 5 contact points: the wall, two particles above, and two particles below. The arrangement is still planar. For $\delta > \delta_c$, the arrangement stops to be planar and the particles arrange in a spiral. Our DEM packings present in some cases deviation from ideal packings that can arise during the pouring process when a particle is blocked by another one before reaching its equilibrium position.

For larger δ , the arrangement tends to be more and more random although some structures can appear. For example, for $\delta > 2$, the particles can form rings and the packings present a “hole” in the center whose size is maximum near $\delta = 2.6$. The hole in the center disappears for higher δ as the probability of a particle being stable in the center increases, which prevents the regular ring formation. A similar rings and holes structure occurs for $\delta \sim 3.4$. The reactor-to-sphere diameter δ governs the packing and small changes of its value can lead to significantly different arrangements.

Table 1. Packing structures for chosen values of δ . Particles are in white and the fluid zone is colored by velocity magnitude (red = fastest flow, blue = slowest flow, the scale is different for each case)

δ	1.06	1.72	2.21	2.58	3.1	3.37	3.875
Structure	Almost planar with passages on the side		Ring and hole in the center		Uniform	Some preferential passages	Uniform
Reactor's cut in the central vertical plane							

An outcome of this non-monotonic behavior is that great care must be taken when using literature correlations near “geometric” transitions. Figure 7 compares the void fraction measured from our DEM simulations to the void fraction predicted by the correlation proposed by Dixon for spheres [36] and the void fraction of some experimental estimations in literature and resumed by Seckendorff et al. [37] in their article. As we can see, there is a good matching until $\delta \sim 1.87$, then for higher values the correlation is not able to capture packing defects. For $\delta > 1.87$ the correlation shows a stable decrease in ε while the data from DEM present some “rebounds” due

to packing imperfections. In the experimental works, these “rebounds” are indeed detected (see Figure 7).

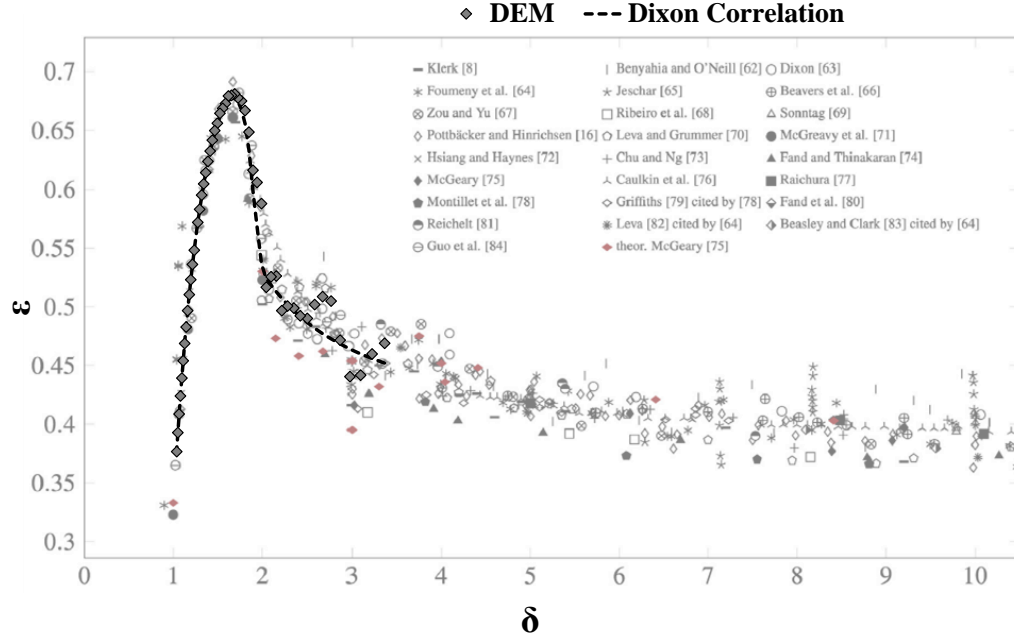


Figure 7. Void fraction as a function of δ in packed beds of spheres measured by DEM (blue diamonds) compared to the Dixon correlation (red line) [36] and other experimental works in literature [37]

Moreover, also the correlations that predict the radial void fraction profile deviate for some specific values of δ . For example, the correlations proposed by Mueller [4] do not predict a hole ($\varepsilon = 1$) in the reactor center for $\delta \sim 2.6$ (Figure 8, $r/d_p = 0$ corresponds to the reactor wall). For that case, some experimental data are present in the literature [38].

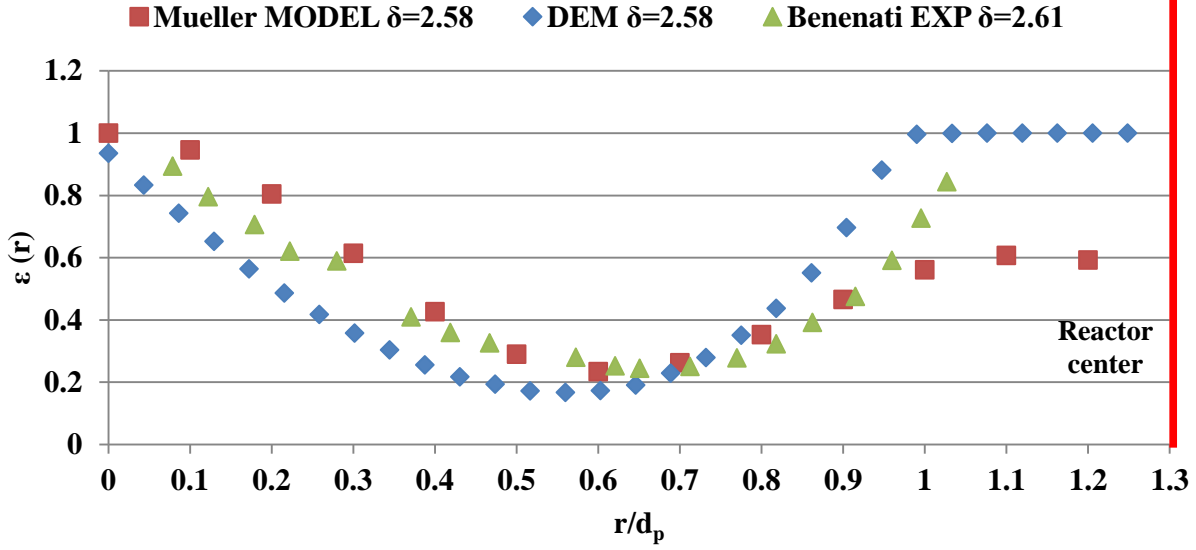


Figure 8. Comparison between radial void fraction profiles measured experimentally [38], Mueller correlation [4], and our DEM results

From our DEM work, we conclude that classical correlations on overall and radial void fraction should be used carefully for values of $\delta > 1.87$ and in particular near geometrical transitions located at $\delta = \delta_c$, $\delta \sim 2.6$ (single ring), and for the values of δ leading to other ring formations ($\delta \sim 3.4$).

3.1.3 Results in narrow reactors for a fixed reactor length

In this section, we use our DEM + CFD workflow to predict Pe_{ax} numbers in narrow reactors filled with spherical particles, varying the geometry through the particles size, inlet velocity and molecular diffusion. The reactor diameter is set to 7.75 mm and its length to 107.3 mm.

The Pe_{ax} number profiles against δ are presented in Figure 9, for various combinations of fluid velocity and molecular diffusion coefficient. The profile is more complex than the one expected

based on our experimental work and depends both on δ and on the combination of velocity and molecular diffusion.

A first comment is that, for the most part of conditions examined, (specifically $Pe_m < 3-4$) doubling the velocity or halving the molecular diffusivity coefficient has the same effect on the Pe_{ax} and Bo number values. This suggests that u/D_m is invariant. However, this is not true for higher values of Pe_m number because of the intervention of the Schmidt number effect [6].

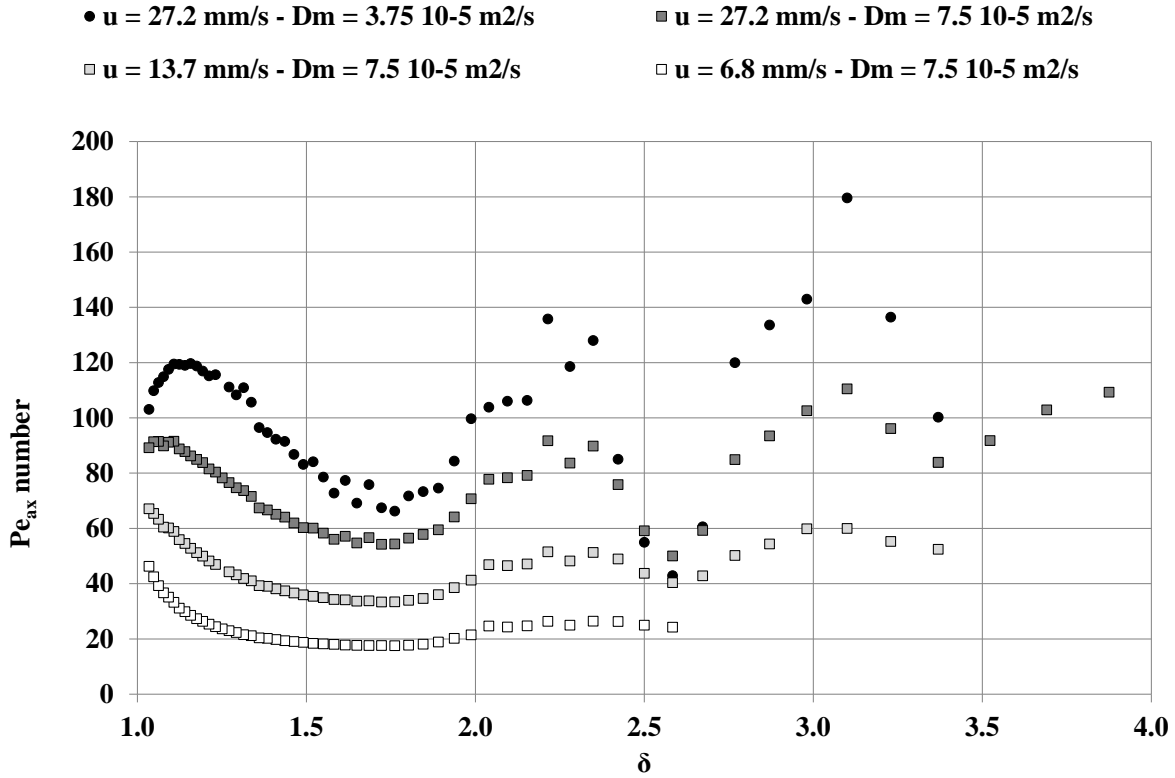


Figure 9. Evolution of Pe_{ax} number against δ for various superficial velocities and molecular diffusivity values. $D_r = 7.75$ mm, $L = 10.73$ cm

Let us first explore in detail the profile of the top curves of Figure 9 (highest velocity and lowest molecular diffusivity, dark symbols). Starting from δ just above 1, the Pe_{ax} number evolution

presents a smooth evolution as the geometrical constraints prevent random packing defects. The reactor Pe_{ax} number value starts at a high value, increases to a maximum ($\delta \sim 1.2$) and then decreases towards a minimum located near $\delta = 1.72$, which is slightly less than the critical value. We explain the gradual decrease of Pe with δ by the progressive increase of the passages on the particle sides that act as bypasses. As it can be seen from

Table 1, the packings are not ideal for $\delta = 1.72$ with a change in the orientation of the particle settling planes due to packing “defects”. Those random effects explain why the Pe_{ax} number starts to increase for $\delta < \delta_c$, in other words before the transition to “spiral” packings that present less opportunities for bypasses. For $\delta > \delta_c$, the Pe_{ax} number increases until the hole at the center of the geometry becomes large enough to create a significant bypass whose consequence on the Pe_{ax} number depends on the velocity and molecular diffusion. The Pe_{ax} number reaches a minimum near $\delta = 2.6$. The “irregularities” in the curve are due to defects in the packing that locally create or prevent bypasses. For larger δ , the Pe_{ax} number increases again due to a more random arrangement less likely to create by-passes. The rest of the curve is a repetition of the latter part: decrease due to a significant preferential path in the center ($\delta \sim 3.4$) followed by an increase due to more random and uniform arrangements and less bypasses.

When the ratio fluid velocity to molecular diffusion decreases, the Pe_{ax} number values are shifted downward. The curves are smoother, and the oscillations get smoother (Figure 9). The smoothing and dampening are explained by a higher contribution of molecular diffusion

compared to velocity. Molecules have more time to diffuse in and out of the bypass. Two length scales are governing the physics: one in the axial direction (particle size or reactor length), one in the radial direction (fluid passage size).

The behavior of the reactors for δ very close to 1 ($1 < \delta < 1.3$) is also different: there is a maximum that is shifted towards lower δ values and it is less pronounced when reducing the fluid velocity (or increasing the molecular diffusivity). In that range of δ , the particles are arranged in a plane (indicated with a dashed line in Figure 10) and the flow patterns are of two types: one type that flows outside of the particles plane (and that becomes more important for larger δ values) and one type that flows in-plane, going from one side of the reactor to the other around the particles. As we can see from Figure 10, for $\delta = 1.1$ most of the flow is in-plane while increasing δ (1.5 in Figure 10) the flow becomes more out of plane.

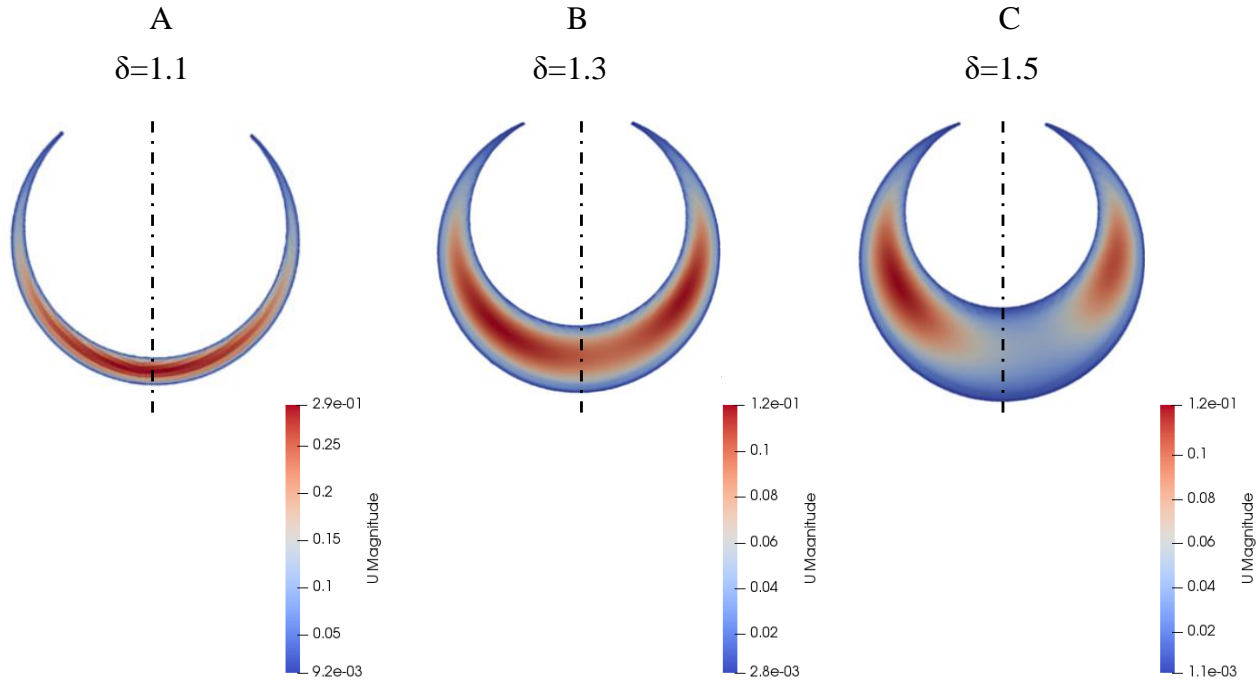


Figure 10. Velocity magnitude in cross sections as a function of the δ value. The cross sections pass through a sphere center. The symmetry plane is indicated with a dashed line. $u = 0.0272$ m/s, $D_r = 7.75$ mm, $D_m = 7.5 \times 10^{-5}$ m²/s. Red = fastest flow, blue = slowest flow

We propose that the change in behavior with velocities and molecular diffusion coefficient is due to the relative change in the importance and interaction of those two flow pattern types.

3.1.4 Comparison with literature on larger packed beds

In the literature, results are traditionally presented as $Bo = f(Pe_m)$ [6], which scales all dimensions to the particle diameter. In Figure 11, we plot the results reported by Delgado [6] for single phase gas flow as well as our results. For clarity, we decided to split our results into three groups.

The first group (Figure 11-A) corresponds to reactors whose Bo numbers are in line with the literature. This group corresponds to $\delta > \delta_c = 1.87$, except for the reactors with large preferential passages or holes in the center ($2.4 < \delta < 2.7$, $\delta = 3.37$).

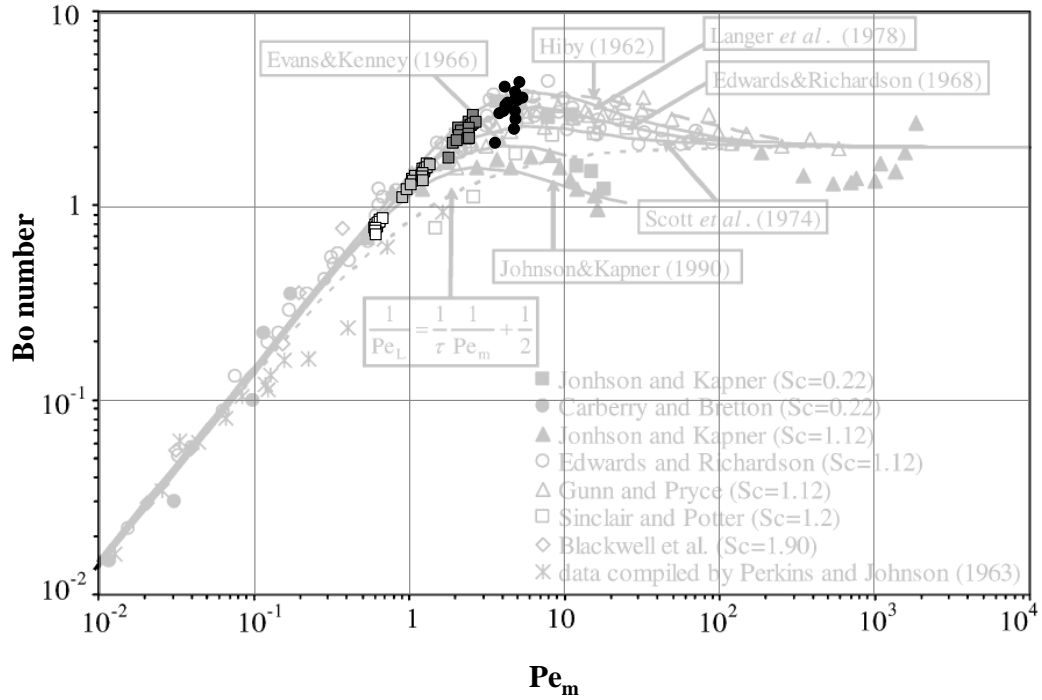
The next group (Figure 11-B) corresponds to reactors with a hole or large preferential passages in the center ($2.4 < \delta < 2.7$, $\delta = 3.37$). At low Pe_m number values ($Pe_m < 2$), in the molecular diffusion driven dispersion zone, these reactors present a similar behavior as group A. But when Pe_m increases, the Bo number of these reactors falls under that of group A: Pe_m is then large enough that the preferential paths in the reactor's center lower the Bo number.

The last group (Figure 11-C) encompasses all reactors with $\delta < \delta_c = 1.87$ that we will denote as Single Pellet String Reactors (SPSRs). These SPSRs present high Bo number values (> 5), particularly for the reactors with $\delta < 1.3$. Our values are similar to those of the experimental study of Šolcova and Schneider [10] for $\delta = 1.25$, as discussed in §2.3. We think that these high

values result mostly from the dimension scaling that is based on the particle diameters, which is quite large in our simulations and Šolcova and Schneider [10] experiments ($d_p > 7$ mm). A more physical scaling based on fluid passage size (hydraulic diameter for example) would bring these data points closer to group A. For larger δ , the passage size is a weak function of the void fraction and the scaling by particle diameter offsets the curve by a constant amount.

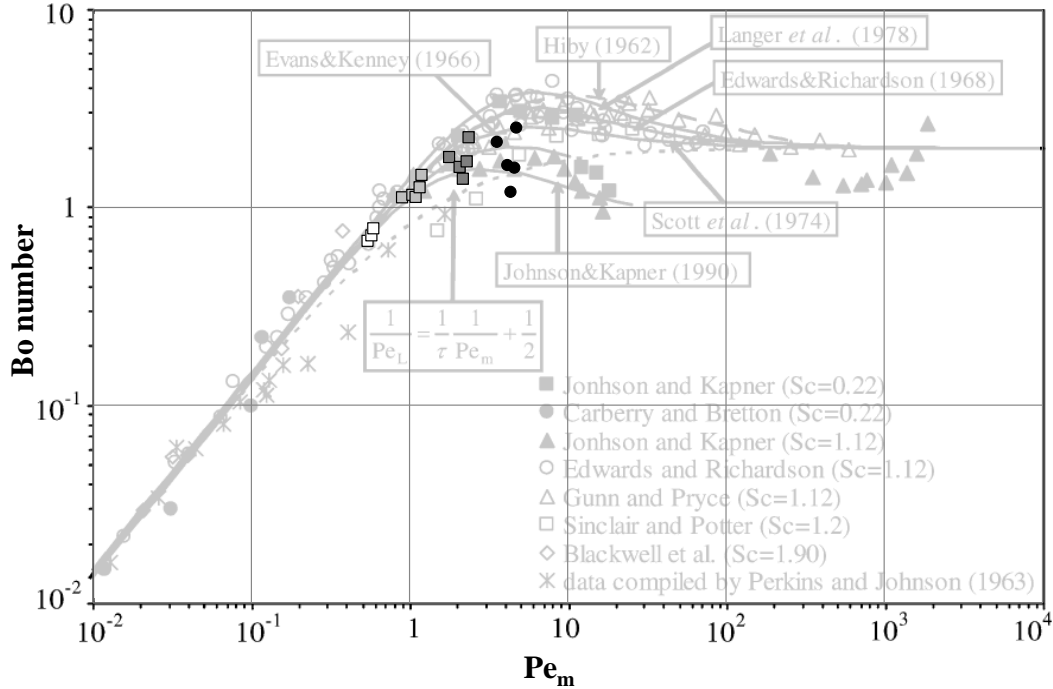
A)

- $u = 27.2 \text{ mm/s}$ - $Dm = 3.75 \cdot 10^{-5} \text{ m}^2/\text{s}$ ■ $u = 27.2 \text{ mm/s}$ - $Dm = 7.5 \cdot 10^{-5} \text{ m}^2/\text{s}$
- ▣ $u = 13.7 \text{ mm/s}$ - $Dm = 7.5 \cdot 10^{-5} \text{ m}^2/\text{s}$ □ $u = 6.8 \text{ mm/s}$ - $Dm = 7.5 \cdot 10^{-5} \text{ m}^2/\text{s}$



B)

- $u = 27.2 \text{ mm/s}$ - $Dm = 3.75 \cdot 10^{-5} \text{ m}^2/\text{s}$ ■ $u = 27.2 \text{ mm/s}$ - $Dm = 7.5 \cdot 10^{-5} \text{ m}^2/\text{s}$
- ▣ $u = 13.7 \text{ mm/s}$ - $Dm = 7.5 \cdot 10^{-5} \text{ m}^2/\text{s}$ □ $u = 6.8 \text{ mm/s}$ - $Dm = 7.5 \cdot 10^{-5} \text{ m}^2/\text{s}$



C)

- $u = 27.2 \text{ mm/s}$ - $D_m = 3.75 \cdot 10^{-5} \text{ m}^2/\text{s}$ ■ $u = 27.2 \text{ mm/s}$ - $D_m = 7.5 \cdot 10^{-5} \text{ m}^2/\text{s}$
- ▣ $u = 13.7 \text{ mm/s}$ - $D_m = 7.5 \cdot 10^{-5} \text{ m}^2/\text{s}$ □ $u = 6.8 \text{ mm/s}$ - $D_m = 7.5 \cdot 10^{-5} \text{ m}^2/\text{s}$

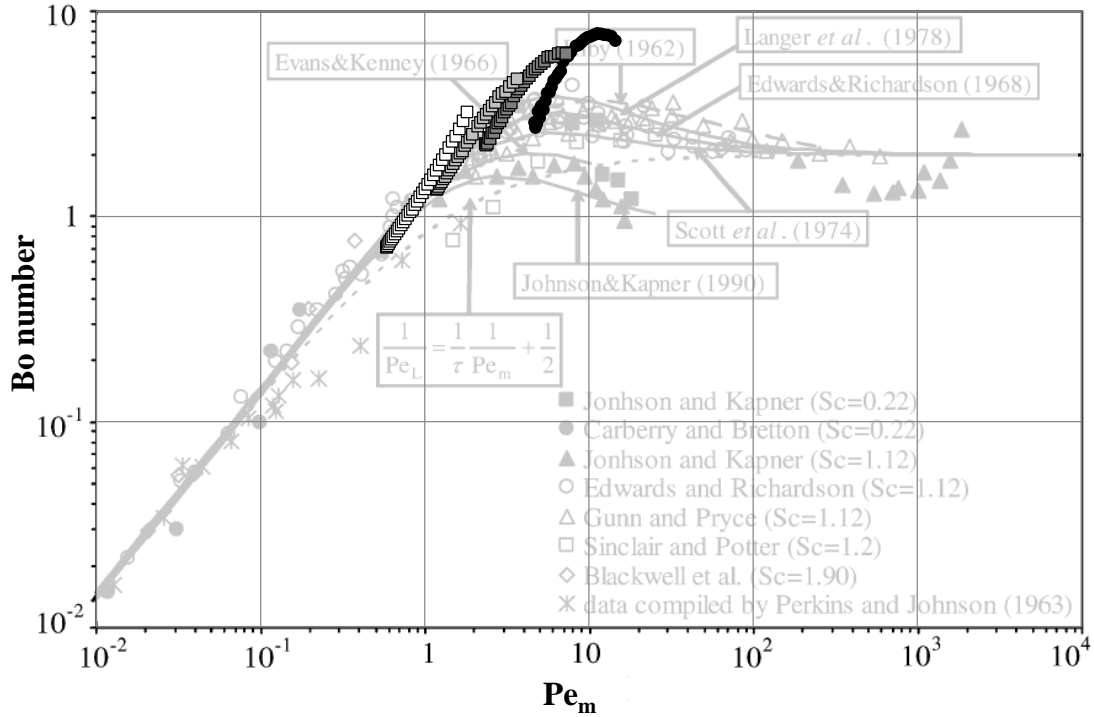


Figure 11. Evolution of the Bo number versus the Pe_m number for various superficial velocities, molecular diffusivities, and bed geometries. A) $1.87 < \delta < 2.4 + 2.7 < \delta < 3.3$, B) $2.4 < \delta < 2.7 + \delta = 3.37$, C) $1.03 < \delta < 1.87$. $D_r = 7.75 \text{ mm}$

3.2 Repeatability of the axial Péclet number profiles in narrow reactors

3.2.1 Methods

We now focus on the variability when repeating the packing in random packed beds. We will compare the Pe_{ax} number profiles along the reactor length for beds packed with the same set of particles but loaded differently through a different set of initial conditions (random seed). For different random seeds, the bed structure can be different due to the stochastic loading even if the particles composing the bed are the same.

As seen earlier, the Pe_{ax} number curves for small δ are smooth as the geometrical constraints limit the probability of defects occurring during packing. We now study larger fixed beds made with 3 mm diameter spheres packed in a 12 mm diameter reactor ($\delta = 4$). We repeat the workflow six times (DEM-CFD) from scratch, to obtain six different packings and check that the packings were really all different and not a rotated version of one another. The easiest way to check this is to sort particles by their center's height (z_i), plot z_i against their rank and check that the curves are not identical. One may also compare void fraction on several slices.

3.2.2 Axial Péclet number profiles in repeated packed beds

The Pe_{ax} number evolution with the reactor axial coordinate z (see Equation 11) follows a linear overall trend consistent with an axial dispersion independent on the length (Figure 12 A). It presents small variations around this trend and these variations are different in all the packings. In the cases presented in Figure 12 A, there is almost no difference at $z = 10$ cm, while a difference of 10 in Pe_{ax} number is measured at $z = 7$ cm. Such a difference can yield significant differences in the apparent reactor performance for high conversion reactions if the Pe_{ax} number is low ($Pe_{ax} < 40$ for example). It depends on the desired conversion [7].

The Pe_{ax} numbers for all the six cases tested are shown in Figure 12 B for four different lengths.

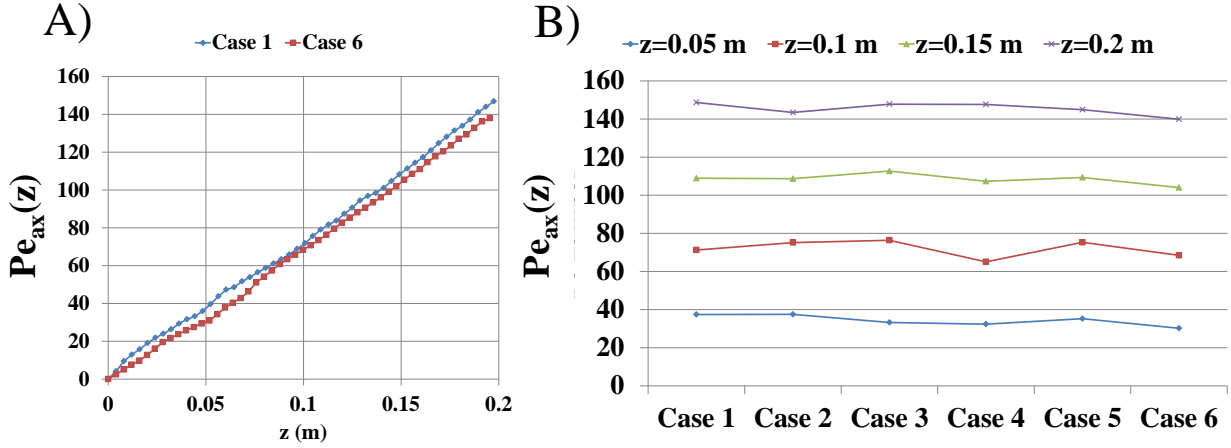


Figure 12. A) Plots of $Pe_{ax}(z)$ number as function of the length in the reactor for two repeats of the same numerical experiment (both beds are made with the same beads and are different). B) $Pe_{ax}(z)$ number variation for the six cases and for four values of the axial coordinate z . $D_m=10^{-6} \text{ m}^2/\text{s}$

A better view of the variability is achieved when plotting the $Pe_{ax}(z)$ number increments (ΔPe) from plane to plane as shown in Figure 13 for case 2 that presents a locally flat evolution of the $Pe_{ax}(z)$ number. The ΔPe value depends on the distance between two cut planes dz (here $dz = 4$ mm). $Pe_{ax}(z)$ number increments in that case are mostly between 1.5 and 2 with slightly higher values but significantly lower values. Lower values (as near $z = 0.13$ m) are due to a hole in the packing and a resulting preferential path of fluid.

We will now propose a method to quantify this variability as a function of the length, which can be useful to design reactors.

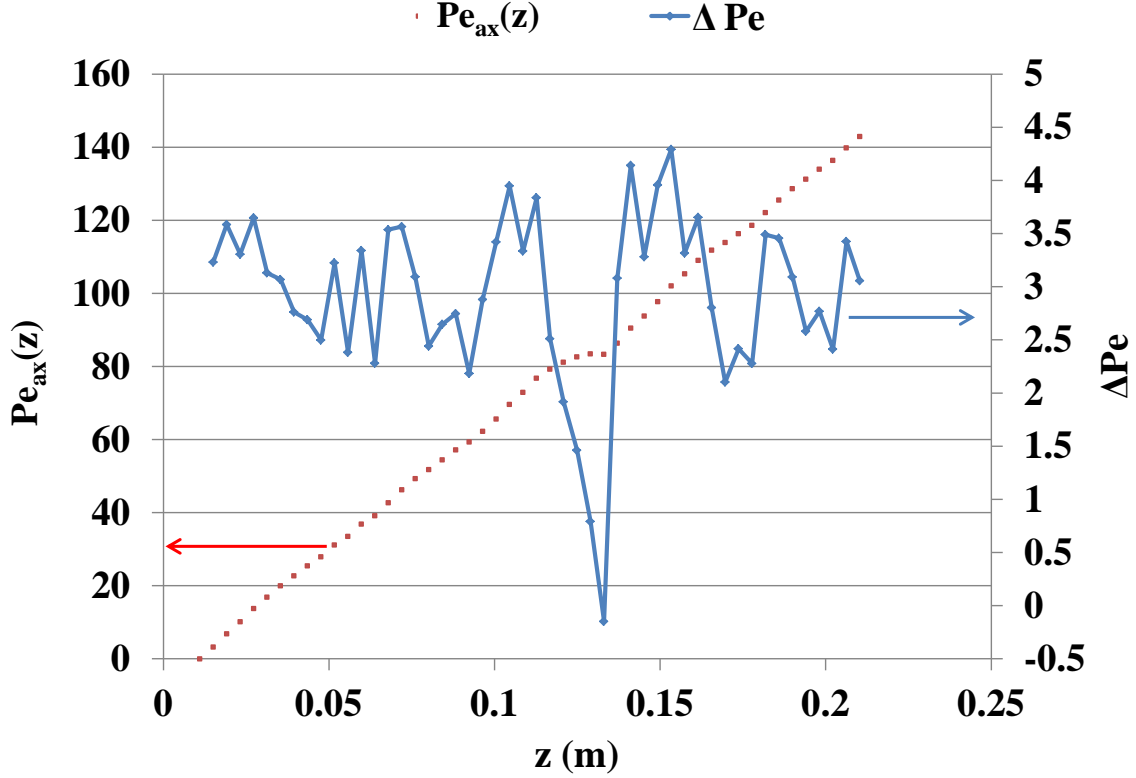


Figure 13. Case 2 - Left axis (red, dashed line): $Pe_{ax}(z)$ number evolution. Right axis (blue): Evolution of the $Pe_{ax}(z)$ number increment ΔPe as a function of reactor length ($dz = 4 \text{ mm}$). $D_m = 10^{-6} \text{ m}^2/\text{s}$

3.2.3 The axial Péclet number uncertainty as a function of the reactor length

We assume that ΔPe is a random variable with a probability density. We can estimate the Pe_{ax} numbers for a reactor of a given length L as the sum of N realizations of the ΔPe random variable, N being the number of Pe_{ax} number increment (L/dz). We will assume that the Pe_{ax} number increment follows a Gaussian law of mean m and standard deviation s . The Pe_{ax} number then follows a Gaussian law of mean $mPe = N \cdot m$ and standard deviation $sPe = s\sqrt{N}$. The relative uncertainty of the Pe_{ax} number with a 95% confidence level $U_{95\%}$ is by definition given by Equation 12. As L is proportional to N , $U_{95\%}$ is proportional to $\frac{1}{\sqrt{L}}$ (Equation 13).

$$U_{95\%} = 1.96 \frac{s_{Pe}}{m_{Pe}} \quad \text{Equation 12}$$

$$U_{95\%} = 1.96 \frac{s\sqrt{N}}{N m} \sim 1.96 \frac{s\sqrt{L}}{L m} \sim \frac{1}{\sqrt{L}} \quad \text{Equation 13}$$

The relative uncertainty on the Pe_{ax} number due to a random packing decreases as the inverse of the square root of the reactor length. Short reactors are thus likely to give both small Pe_{ax} numbers and large variations of Pe_{ax} number values and are thus not recommended for kinetic studies.

4 Conclusions

Combining recent advances in fixed bed simulations and Liu and Tilton moments of the age distribution theory [24], we were able to compute accurate values of Pe_{ax} number in fixed bed reactors packed with spheres in presence of a single-phase laminar flow. The whole workflow is fully automated and requires less than 1 day per case (geometry creation, meshing, CFD simulation and post-treatment). This workflow is now faster than experiments and allows for a good control on parameters. It gives access to local information as would be given by complex experimental tools like μ PIV or tomography.

We first used this capability to explore the relationship of the Pe_{ax} number as a function of δ for narrow reactors ($\delta < 4$), fluid velocity and molecular diffusivity. This relationship proves to be quite complex and it can be qualitatively explained by looking at the packing structures. The Pe_{ax} number is lower when the structures present large preferential passages or holes. This happens for values of δ around 1.7, 2.6 and 3.4.

Then, we used the DEM-CFD workflow to quantify the packing uncertainty in a $\delta = 4$ fixed bed reactor. Repeating the packing has an effect on local preferential passages or “defects” that influence the Pe_{ax} number. While, as already known, the Pe_{ax} number increases on average linearly with the length, we propose that the uncertainty on the Pe_{ax} number decreases with a power of -0.5 of the reactor length.

Nomenclature

Roman letters

a:	Age of the molecules	[s]
c:	Concentration	[mol/m ³]
cpd:	Cells per diameter	
D _{ax} :	Axial dispersion coefficient	[m ² /s]
D _m :	Molecular diffusivity	[m ² /s]
d _p :	Particles diameter	[m]
D _r :	Reactor internal diameter	[m]
dz:	Spatial discretization interval	[m]
E(t):	Normalized response to a Dirac function	[s ⁻¹]
L:	Bed length	[m]
m:	Mean of a gaussian distribution variable	
M ₁ :	First order moment of the E(t)	[s]
M ₂ :	Second order moment of the E(t)	[s ²]
n:	Generic moments order	
N:	Number of realizations of ΔPe increment	

Q:	Gas flow rate	[m ³ /s]
r:	Reactor radial coordinate	[m]
s:	Standard deviation of a gaussian distribution variable	
S:	Generic surface	[m ²]
SV:	Space Velocity	[s ⁻¹]
t:	Time	[s]
\bar{t} :	Mean fluid residence time	[s]
u:	Inlet superficial velocity	[m/s]
U95%:	Relative 95% confidence level uncertainty	
V _{cat} :	Catalyst volume	[m ³]
x:	Generic point in the reactor	
z:	Reactor axial coordinate	[m]

Greek letters

$\delta: \frac{D_r}{d_p}$	Reactor/particle diameter ratio
$\Delta Pe:$	Difference in Pe number between two reactor plans

ε :	Void fraction of the reactor	
μ :	Fluid viscosity	[Pa·s]
ρ :	Fluid density	[kg/m ³]
σ :	Variance	[s ²]
τ :	Tortuosity factor of the packed bed	

Dimensionless numbers

$Bo: \frac{u \cdot d_p}{\varepsilon \cdot D_{ax}}$	Bodenstein number
$Pe_{ax}: \frac{u \cdot L}{\varepsilon \cdot D_{ax}}$	Axial Peclet number
$Pe_m: \frac{u \cdot d_p}{\varepsilon \cdot D_m}$	Molecular Peclet number
$Re: \frac{\rho \cdot u \cdot d_p}{\varepsilon \cdot \mu}$	Reynolds number
$Sc: \frac{\mu}{\rho \cdot D_m}$	Schmidt number

References

- 1 Moulijn J., Pérez-Ramírez J., Berger R., Hamminga G., Mul G., Kapteijn F. (2003) High-throughput experimentation in catalyst testing and in kinetic studies for heterogeneous catalysis, *Catalysis Today*, Vol. 81 No. 3, Pag. 457–471. DOI: 10.1016/S0920-5861(03)00145-7.
- 2 Chu C. F., Ng K. M. (1989) Flow in packed tubes with a small tube to particle diameter ratio, *AIChE Journal*, Vol. 35, No. 1.
- 3 McGearry R.K. (1961) Mechanical packing of spherical particles, *Journal of the American Ceramic Society*, Vol. 44 No. 10, Pag. 513-522.
- 4 Mueller G.E. (1992) Radial void fraction distributions in randomly packed fixed beds of uniformly sized spheres in cylindrical containers, *Powder Technology*, Vol. 72 No. 3, Pag. 269–275. DOI: 10.1016/0032-5910(92)80045-X.
- 5 Bellos G.D., Gotsis K.P., Papayannakos N.G. (2007) The gas–liquid contacting effect on the operation of small scale upflow hydrotreaters, *Catalysis Today* **127**, 1-4, 103–112. DOI: 10.1016/j.cattod.2007.05.004.
- 6 Delgado J. (2006) A critical review of dispersion in packed beds, *Heat Mass Transfer*, Vol. 42 No. 4, Pag. 279–310. DOI: 10.1007/s00231-005-0019-0.
- 7 Mears D.E. (1971) Diagnostic criteria for heat transport limitations in fixed bed reactors, *Journal of Catalysis*, Vol. 20, Pag. 127-131.
- 8 Edwards M. F. and Richardson J. F. (1968) Gas dispersion in packed beds, *Chemical Engineering Science*, Vol. 23, Pag. 109-123.
- 9 de Carvalho, J. R. F. Guedes, Delgado, J. M. P. Q. (2003) Effect of fluid properties on dispersion in flow through packed beds, *AIChE J.* **49**, 8, 1980–1985. DOI: 10.1002/aic.690490808.
- 10 Šolcova O., Schneider P. (2004) Axial dispersion in single pellet-string columns with non-porous packing, *Chemical Engineering Science*, Vol. 59 No. 6, Pag. 1301–1307. DOI: 10.1016/j.ces.2004.01.011.
- 11 Kallinikos L.E., Papayannakos N.G. (2007) Fluid dynamic characteristics of a structured bed spiral mini-reactor, *Chemical Engineering Science* **62**, 21, 5979–5988. DOI: 10.1016/j.ces.2007.06.006.
- 12 Hipolito A.I., Rolland M., Boyer C., Bellefon C. de (2010) Single Pellet String Reactor for Intensification of Catalyst Testing in Gas/Liquid/Solid Configuration, *Oil Gas Sci. Technol. – Rev. IFP Energies nouvelles* **65**, 5, 689–701. DOI: 10.2516/ogst/2009079.
- 13 Scott D.S., Lee W. and Papa J. (1974) The measurement of transport coefficients in gas-solid heterogeneous reactions, *Chemical Engineering Science*, Vol. 29, Pag. 2155-2167.
- 14 Hsiang, T.C.S. and Haynes Jr, H.W. (1977) Axial dispersion in small diameter beds of large, spherical particles, *Chemical Engineering Science*, Vol 32, Pag. 678-681.
- 15 Petrazzuoli V., Rolland M., Mekki-Berrada A., Said-Aizpuru O., Schuurman Y. (2021) Choosing the right packing in packed bed millireactors under single phase gas flow, *Chemical Engineering Science* **Vol. 231**, Article 116314.
- 16 Augier F., Idoux F., Delenne J.-Y. (2010) Numerical simulations of transfer and transport properties inside packed beds of spherical particles, *Chemical Engineering Science* **Vol. 65 No. 3**, Pag. 1055-1064.

- 17 Michiel Nijemeisland, Anthony G. Dixon (2004) CFD Study of fluid flow and wall heat transfer in a fixed bed of spheres, *AIChE Journal*, Vol. 50, Pag. 906–921.
- 18 Partopour B., Dixon A.G. (2017) An integrated workflow for resolved-particle packed bed models with complex particle shapes, *Powder Technology*, Vol. 322, Pag. 258–272.
- 19 Pozzobon V., Colin J., Perré P. (2018) Hydrodynamics of a packed bed of non-spherical polydisperse particles: A fully virtual approach validated by experiments, *Chemical Engineering Journal* **354**, 126–136. DOI: 10.1016/j.cej.2018.07.214.
- 20 Boccardo G., Augier F., Haroun Y., Ferré D., Marchisio D.L. (2015) Validation of a novel open-source work-flow for the simulation of packed-bed reactors, *Chemical Engineering Journal* **279**, 809–820. DOI: 10.1016/j.cej.2015.05.032.
- 21 Sassanis V., Gamet L., Rolland M., Ma R., Pozzobon V. (2020) Numerical determination of the volumetric heat transfer coefficient in fixed beds of wood chips, *Chemical Engineering Journal*. DOI: 10.1016/j.cej.2020.128009.
- 22 A. Müller, J. Petschick, R. Lange (2012) Model-Based Investigation of a Pellet String Reactor, *Procedia Engineering*, Vol. 42, Pag. 1189-1201.
- 23 Fernengel J., Bolton L., Hinrichsen O. (2019) Characterisation and design of single pellet string reactors using numerical simulation, *Chemical Engineering Journal* **373**, 1397–1408. DOI: 10.1016/j.cej.2019.03.114.
- 24 Liu M., Tilton J.N. (2010) Spatial distributions of mean age and higher moments in steady continuous flows, *AIChE J.* **56**, 10, 2561–2572. DOI: 10.1002/aic.12151.
- 25 Spalding D. B. (1958) A note on mean residence-times in steady flows of arbitrary complexity, *Chemical Engineering Science*, Vol. 9 No.1, Pag. 74-77.
- 26 Danckwerts P. V. (1958) The effect of incomplete mixing on homogeneous reactions, *Chemical Engineering Science*, Vol.8 No. 1-2, Pag. 93-102.
- 27 Zwietering Th. N. (1959) The degree of mixing in continuous flow systems, *Chemical Engineering Science*, Vol. 11 No. 1, Pag. 1-15.
- 28 Cundall, Peter A. and Otto DL Strack (1979) A discrete numerical model for granular assemblies, *Geotechnique* **Vol.29 N.1**, Pag. 47-65.
- 29 Gilbert E. G., Johnson D. W., Keerthi S. S. (1988) A fast procedure for computing the distance between complex objects in three-dimensional space, *IEEE Journal of robotics and automation*, Vol. 4 No. 2, Pag. 193-203.
- 30 Wachs A., Girolami L., Vinay G., Ferrer G. (2012) Grains3D, a flexible DEM approach for particles of arbitrary convex shape—Part I: Numerical model and validations, *Powder Technology*, Vol. 224, Pag. 374–389.
- 31 OpenFOAM Foundation OpenFOAM user guide - snappyHexMesh. Available at: <https://cfd.direct/openfoam/user-guide/v6-snappyhexmesh/>.
- 32 OpenFOAMWiki The openFOAM simpleFoam solver. Available at: <https://openfoamwiki.net/index.php/SimpleFoam>.
- 33 OpenCFD E.S. OpenFOAM, the open source CFD toolbox, user guide. Available at: <http://www.openfoam.com/documentation/user-guide>.

- 34 Dixon A.G., Ertan Taskin M., Nijemeisland M., Stitt E.H. (2011) Systematic mesh development for 3D CFD simulation of fixed beds: Single sphere study, *Computers & Chemical Engineering* **Vol. 35**, Pag. 1171–1185. DOI: 10.1016/j.compchemeng.2010.12.006.
- 35 Rolland M., Rakotonirina A.D., Devouassoux A., Barrios G. J.L., Delenne J.-Y., Wachs A. (2019) Predicting average void fraction and void fraction uncertainty in fixed beds of poly lobed particles, *Ind. Eng. Chem. Res.*, Vol. 58, Pag. 3902–3911. DOI: 10.1021/acs.iecr.8b05557.
- 36 Dixon A.G. (1988) Correlations for wall and particle shape effects on fixed bed bulk voidage, *Can. J. Chem. Eng.* **66**, 5, 705–708. DOI: 10.1002/cjce.5450660501.
- 37 Seckendorff J. von, Achterhold K., Pfeiffer F., Fischer R., Hinrichsen O. (2021) Experimental and numerical analysis of void structure in random packed beds of spheres, *Powder Technology* **Vol. 380**, Pag. 613–628. DOI: 10.1016/j.powtec.2020.11.026.
- 38 R. F. Benenati and C. B. Brosilow (1962) Void fraction distribution in beds of spheres, *AIChE Journal*, Vol. 8 No. 3, Pag. 359-361.